J. Plasma Phys. (2023), *vol*. 89, 905890310
Published by Cambridge University Press
doi:10.1017/S002237782300051X

Centrifugal instability in a weakly magnetized rotating plasma column

S. Aggarwal[1],†, **Y. Camenen**[1], **A. Escarguel**[1] **and A. Poyé**[1]

[1]Aix-Marseille Université, CNRS, PIIM UMR 7345, Marseille, France

(Received 19 January 2023; revised 22 May 2023; accepted 23 May 2023)

A two-fluid model is developed to study the stability of weakly magnetized rotating plasma columns. Previous works have shown that rotating plasma columns are prone to centrifugal flute modes. Most of these models are based on the low-frequency assumption which is valid when the instability frequency and the plasma azimuthal frequency are small compared with the ion cyclotron frequency. This assumption is challenged in many laboratory plasma devices, including weakly magnetized plasma columns. A radially global dispersion relation relaxing the low-frequency approximation and applicable in these devices is derived. The validity domain of the low-frequency approximation is discussed. In addition, the impact of the radial boundary on the linear stability is investigated and comparison with results obtained in the radially local approximation are performed.

Keywords: plasma instabilities, plasma dynamics

1. Introduction

A canonical configuration for the study of weakly magnetized plasmas is a cylindrical plasma column immersed in an axial magnetic field. Here, weakly magnetized is understood as a plasma radius of typically 3 to 30 ion Larmor radii. The presence of a radial electric field E_r or a radial gradient of the plasma pressure perpendicular to the magnetic field leads to flows in the azimuthal direction. These flows, when combined with plasma inhomogeneities (density or temperature gradients), give rise to various instabilities resulting in turbulence, the appearance of coherent structures and anomalous transport which generally affect the performance of the device.

Understanding the formation of large-scale structures in weakly magnetized plasmas is of particular interest for both fundamental research and technological applications like magnetron sources (Abolmasov 2012), Penning discharges (Ellison, Raitses & Fisch 2012) and negative ion sources. Rotating coherent structures have also been observed in Hall thrusters (Sekerak *et al.* 2015; Parker, Raitses & Fisch 2010) where they are called 'spokes' and limit the performance of the device.

In the past decades, many models have been proposed to study instabilities in $E \times B$ plasmas, where B is the magnetic field (Rosenbluth, Krall & Rostoker 1962; Chen 1966; Stringer & Schmidt 1967; Lehnert 1971; Perkins & Jassby 1971; Jassby 1972; Ilić *et al.*

† Email address for correspondence: surabhi.aggarwal@univ-amu.fr

1973; Rognlien 1973; Smolyakov *et al.* 2016; Gueroult, Rax & Fisch 2017). Rosenbluth *et al.* (1962) have explained the stability of a rotating cylindrical plasma column in the frame of kinetic theory, valid for a low β plasma, where β is the ratio of plasma pressure to the magnetic pressure, for $k\rho_i < 1$ and $\omega/\omega_{ci} \approx (k\rho_i)^2$, where ω is the plasma perturbation frequency, ω_{ci} is the ion-cyclotron frequency, k is the wave vector of the perturbation and ρ_i is the ion Larmor radius. Terms of the order of $(k\rho_i)^2$ have been retained and higher-order terms have been neglected. Rotating plasma columns were shown to be prone to the centrifugal instability that stems from the difference between the azimuthal velocity of ions and electrons caused by inertia.

Chen (1966) verified the results of Rosenbluth *et al.* (1962) using a two-fluid model, still, however, under the low-frequency assumption (LFA) i.e. $\omega_{ph} \ll \omega_{ci}$, where ω_{ph} is the Doppler shifted frequency given by $\omega_{ph} = \omega - m\omega_0$. Here, m is the azimuthal mode number and ω_0 is the equilibrium flow frequency of ions. In this treatment, both the mode frequency and equilibrium flow frequency are ordered small, with $\omega_{ph}/\omega_{ci} = O(\rho^2)$, where $\rho \ll 1$ is the magnetization parameter defined as $\rho = \rho_i/l$, with l as the scale length of macroscopic gradients. Chen studied the influence of finite Larmor radius and magnetic shear on the linear stability. He also extended the model to the regime of fast rotation by assuming $\omega_{ph}/\omega_{ci} = O(\rho)$.

As an extension of the above-referenced work, Rognlien (1973) gave analytical and numerical solutions of low-frequency electrostatic waves ($\omega \ll \omega_{ci}$) in a radially bounded plasma column for lower azimuthal mode numbers ($m = 1, 2$) for uniform as well as non-uniform rotation.

Most of the models formulated so far to study $E \times B$ plasmas are based on the LFA ($\omega_{ph} \ll \omega_{ci}$) and therefore not suitable for weakly magnetized linear plasma devices such as MISTRAL (Jaeger 2010), RAID (Furno *et al.* 2017), and VKP (Plihon *et al.* 2014) where the frequency values, ω and ω_0, are typically comparable to the ion-cyclotron frequency ω_{ci}.

Recently, Gueroult *et al.* (2017) have studied the centrifugal instability for an $E \times B$ plasma column in the regime of fast rotation ($|\omega_0 - \omega_{0e}|/\omega_{ci} \approx O(1)$, where ω_{0e} is the equilibrium flow frequency of electrons) with no constraint on the perturbation frequency ω. The analysis was performed in the radially local limit and focused on the case of a radially outward electric field, $E_r > 0$. To the authors' knowledge, no attempt has been made to go beyond the LFA in a radially global model, including the influence of boundary conditions. This is the purpose of the present work. We have verified and extended the results of Chen (1966) and Gueroult *et al.* (2017) to obtain a radially global solution valid at arbitrary frequency. The differences between the radially local and global solutions, with and without LFA, have been explored to clarify the effect of these assumptions. Throughout the paper, the example of MISTRAL is used to highlight typical parameters encountered in linear plasma columns. No direct comparison with experimental measurements is attempted yet since this still requires further model developments.

The plan of the paper is as follows: in § 2, the two-fluid model equations and assumptions are presented. In § 3, the equilibrium flow frequency in the cylindrical geometry is derived. Section 4 details the dispersion relation for the radially global case and in the local limit with and without LFA. In § 5, the linear stability is discussed to highlight the regimes where the instability can be found. In § 6, a comparison between local and global growth rates is made, and in § 7, the summary and conclusions are presented.

https://doi.org/10.1017/S002237782300051X Published online by Cambridge University Press

2. Model equations

We consider a cylindrical plasma bounded radially and immersed in a homogeneous magnetic field such that $\boldsymbol{B} = B\hat{e}_z$ (see figure 1). The model is based on the continuity and momentum equations for electrons and ions

$$\frac{\partial n_j}{\partial t} + \nabla \cdot (n_j \boldsymbol{v}_j) = 0, \tag{2.1}$$

$$n_i m_i \left(\frac{\partial \boldsymbol{v}_i}{\partial t} + \boldsymbol{v}_i \cdot \nabla \boldsymbol{v}_i \right) = n_i e(-\nabla\phi + \boldsymbol{v}_i \times \boldsymbol{B}) - T_i \nabla n_i - m_i n_i \nu_{\text{in}} \boldsymbol{v}_i, \tag{2.2}$$

$$0 = -en_e(-\nabla\phi + \boldsymbol{v}_e \times \boldsymbol{B}) - \nabla(n_e T_e), \tag{2.3}$$

with

$$\nabla = \frac{\partial}{\partial r}\hat{e}_r + \frac{1}{r}\frac{\partial}{\partial \theta}\hat{e}_\theta + \frac{\partial}{\partial z}\hat{e}_z, \tag{2.4}$$

where $\hat{e}_r$, $\hat{e}_\theta$ and $\hat{e}_z$ are the unit vectors in r, θ and z directions, respectively. Here, $j = i, e$ denotes either ions or electrons, n_j is the number density, $\boldsymbol{v}_j$ is the velocity of the species, m_j is the mass of the species, $T_{i,e}$ is the species temperature, ϕ is the electric potential and ν_{in} is the ion–neutral collision frequency. The following assumptions are used:

- Electrostatic approximation, $\partial \boldsymbol{B}/\partial t = 0$.
- Quasi-neutrality, $n_i = n_e$.
- No particle source.
- No variations in the axial direction ($k_\parallel = 0$).
- Radially uniform ion temperature i.e. $T_i \approx 0.1$ eV.
- No Gyroviscosity ($\nabla \cdot \pi_i = 0$, $\nabla \cdot \pi_e = 0$).
- Electron inertia neglected as a consequence of the small mass of electrons i.e. $m_e/m_i \ll 1$.
- Electron collisions with ions and neutrals neglected. This is, for instance, relevant for the regimes met in MISTRAL (Annaratone *et al.* 2011) where ν_{ei}, $\nu_{en}/\omega_{ce} \ll 1$.

The plasma density, flow and electric potential are written as the sum of a time-independent equilibrium part denoted by subscript 0 and a fluctuating part denoted by superscript $\sim$ as $n = n_0 + \tilde{n}$, $\boldsymbol{v} = \boldsymbol{v}_0 + \tilde{\boldsymbol{v}}$ and $\phi = \phi_0 + \tilde{\phi}$, where the fluctuating part has the following form:

$$\left.\begin{aligned} \tilde{n} &= n_1(r)\exp[\mathrm{i}(m\theta - \omega t)] \\ \tilde{\boldsymbol{v}} &= \boldsymbol{v}_1(r)\exp[\mathrm{i}(m\theta - \omega t)] \\ \tilde{\phi} &= \phi_1(r)\exp[\mathrm{i}(m\theta - \omega t)] \end{aligned}\right\}. \tag{2.5}$$

Here, n_0 is the equilibrium density of ions or electrons, ϕ_0 is the equilibrium electric potential and $\boldsymbol{v_0}$ is the equilibrium flow. For the fluctuating part, n_1 and ϕ_1 give the perturbation amplitudes of the density and potential, respectively, $\boldsymbol{v}_1(r) = v_{r_1}\hat{e}_r + v_{\theta_1}\hat{e}_\theta$, v_{r1} and $v_{\theta 1}$ are the radial and azimuthal components of the perturbed velocity, respectively, m is the azimuthal mode number and $\omega = \omega_r + i\gamma$, where ω_r is the mode frequency and γ is the growth rate.

The equilibrium density (n_0) and plasma potential (ϕ_0) are assumed to have Gaussian and parabolic profiles, respectively. This is compatible with typical profiles measured in

https://doi.org/10.1017/S002237782300051X Published online by Cambridge University Press

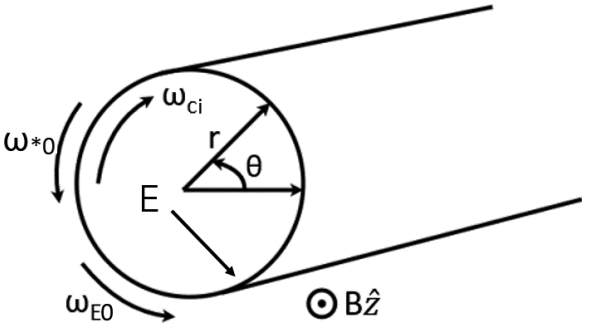

FIGURE 1. Cylindrical coordinate system and direction of rotation for ion-cyclotron frequency $\omega_{\rm ci}$, positive $E \times B$ frequency ($\omega_{E0} > 0$) and positive diamagnetic frequency ($\omega_{*0} > 0$).

MISTRAL (see the Appendix)

$$n_0(r) = n_{00} \exp\left(-\frac{r^2}{r_0^2}\right); \quad \phi_0 = p_1 r^2 + p_2, \tag{2.6a,b}$$

where n_{00}, p_1 and p_2 are constants. Here, r is the radial coordinate and r_0 is the width of the Gaussian used to parametrize the density profile; r_0 characterizes how fast the plasma density decays to zero when moving radially outward. These equilibrium profiles are consistent with the rigid body rotation assumption used for the equilibrium, see § 3.

3. Equilibrium flow

In this section, we derive the expression for the ion equilibrium flow as a function of the $E \times B$ flow and the diamagnetic flow under the assumption of rigid body rotation. The equilibrium flow velocity for ions is first split into radial and azimuthal components

$$\boldsymbol{v_{i0}}(r) = v_{ir_0}\hat{e}_r + v_{i\theta_0}\hat{e}_\theta, \tag{3.1}$$

and rigid body rotation is assumed such that $v_{i\theta_0} = r\omega_0$ with $\omega_0' = \omega_0'' = 0$, where $'$ represents $\partial/\partial r$ and $''$ represents $\partial^2/\partial r^2$. The ion inertial term $\boldsymbol{v_{i0}} \cdot \boldsymbol{\nabla} \boldsymbol{v_{i0}}$ entering (2.2) becomes

$$(\boldsymbol{v}_{i0} \cdot \boldsymbol{\nabla})\boldsymbol{v}_{i0} = \left(v_{ir_0}\frac{\partial v_{ir_0}}{\partial r} - r\omega_0^2\right)\hat{e}_r + 2\omega_0 v_{ir_0}\hat{e}_\theta. \tag{3.2}$$

Substituting equations (3.1) and (3.2) into the ion momentum equation ((2.2)), assuming $\partial \boldsymbol{v}_{i0}/\partial t = 0$, taking the cross-product with $\boldsymbol{B}$ and then projecting along $\hat{e}_r$, one gets

$$v_{ir_0} = \frac{-\nu_{\rm in} r\omega_0}{\omega_{\rm ci} + 2\omega_0}. \tag{3.3}$$

The equation above is normalized by dividing v_{ir_0} with $v_{{\rm th}_i} = \sqrt{T_i/m_i}$; r with $\rho_i = m v_{{\rm th}_i}/eB$; $\nu_{\rm in}$, ω_0 with $\omega_{\rm ci} = eB/m_i$ where the normalized quantities are noted with an overbar, see table 1,

$$\bar{v}_{ir_0} = \frac{-\bar{\nu}_{\rm in}\bar{r}\bar{\omega}_0}{1 + 2\bar{\omega}_0}, \tag{3.4}$$

which is the equilibrium flow of ions in the radial direction.

https://doi.org/10.1017/S002237782300051X Published online by Cambridge University Press

Variable	Notation	Definition
Normalized frequencies	$\bar{\omega}$, $\bar{\omega}_0$	$\omega/\omega_{\rm ci}$, $\omega_0/\omega_{\rm ci}\omega/\omega_{\rm ci}$, $\omega_0/\omega_{\rm ci}$
Normalized lengths	$\bar{r}$, $1/\bar{L}_n$	r/ρ_i, ρ_i/L_n
Normalized perturbed density	$\bar{n}_1$	n_1/n_0
Normalized perturbed potential	$\bar{\phi}_1$	$e\phi_1/T_{e0_{\rm ref}}$
Normalized velocities	$\bar{v}_{i,e}$	$v_{i,e}/v_{\rm thi}$

TABLE 1. Normalized parameters and their definitions. Here, $T_{e0_{\rm ref}}$ is the reference value of the electron temperature.

Using (3.3) in (2.2) and projecting along $\hat{e}_\theta$, the azimuthal flow frequency $\omega_0 = v_{i\theta_0}/r$ is given by

$$\left(\frac{\nu_{\rm in}\omega_0}{2\omega_0+\omega_{\rm ci}}\right)^2 - \omega_0^2 = -\omega_{\rm ci}\omega_{E0} + \omega_{\rm ci}\omega_0 - \omega_{\rm ci}\omega_{*0} + \left(\frac{\nu_{\rm in}^2\omega_0}{2\omega_0+\omega_{\rm ci}}\right). \tag{3.5}$$

Here, ω_{E0} is the $E\times B$ drift frequency

$$\omega_{E0} = \frac{\boldsymbol{B}\times\boldsymbol{\nabla}\phi_0}{rB^2}\cdot\hat{e}_\theta = \frac{\phi_0'}{rB}, \tag{3.6}$$

and ω_{*0} is the ion diamagnetic drift frequency

$$\omega_{*0} = \frac{T_i}{en_0B}\frac{\boldsymbol{B}\times\boldsymbol{\nabla}n_0}{rB}\cdot\hat{e}_\theta = \frac{T_i}{erB}\frac{n_0'}{n_0} \tag{3.7}$$

$$= -\frac{T_i}{erB}\frac{1}{L_n}, \tag{3.8}$$

where $1/L_n = -n_0'/n_0 = 2r/r_0^2$ is the logarithmic density gradient. It should be noted that ω_{E0} and ω_{*0} are independent of r because of the choice of n_0 and ϕ_0 given by (2.6*a*,*b*).

The rotation direction for positive $E\times B$ and diamagnetic frequency is illustrated in figure 1. Azimuthal flows are counted positive in the direction of increasing θ.

The normalized form of (3.5) is

$$4\left(\bar{\omega}_0+\frac{1}{2}\right)^4 - (1-\bar{\nu}_{\rm in}^2+4(\bar{\omega}_{E0}+\bar{\omega}_{*0}))\left(\bar{\omega}_0+\frac{1}{2}\right)^2 - \frac{\bar{\nu}_{\rm in}^2}{4} = 0, \tag{3.9}$$

which is a fourth-order polynomial in $\bar{\omega}_0$ whose solutions are given by

$$\bar{\omega}_0 = \pm\tfrac{1}{2}\sqrt{\tfrac{1}{2}[b+\sqrt{b^2+4\bar{\nu}_{\rm in}^2}]} - \tfrac{1}{2}, \tag{3.10}$$

where $b = 1+4(\bar{\omega}_{*0}+\bar{\omega}_{E0}) - \bar{\nu}_{\rm in}^2$. Equation (3.9) has four roots. Only two roots will be considered since the other two are imaginary and the equilibrium flow is undefined. Equation (3.10) gives the remaining two roots. The branch for which $\bar{\omega}_0$ increases with increasing $\bar{\omega}_{E0}+\bar{\omega}_{*0}$ is the slow rotation mode and the one that decreases with increasing $\bar{\omega}_{E0}+\bar{\omega}_{*0}$ is the fast rotation mode (Rax *et al.* 2015).

The normalized equilibrium flow $\bar{\omega}_0$ is shown in figure 2 as a function of the sum of the normalized $E\times B$ and diamagnetic flows, $\bar{\omega}_{E0}+\bar{\omega}_{*0}$, for different values of $\bar{\nu}_{\rm in}$.

https://doi.org/10.1017/S002237782300051X Published online by Cambridge University Press

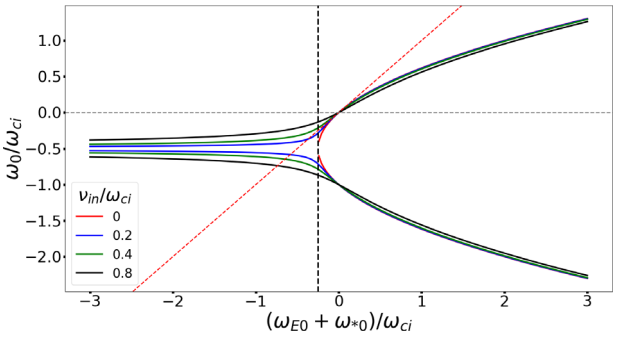

FIGURE 2. Normalized equilibrium flow frequency (ω_0/ω_{ci}) as a function of normalized $E \times B$ drift frequency (ω_{E0}/ω_{ci}) and ion diamagnetic drift frequency (ω_{*0}/ω_{ci}) for different values of normalized ion–neutral collision frequency (ν_{in}/ω_{ci}). The black dashed line presents the stability limit for $\bar{\nu}_{in} = 0$. The red dashed line is the diagonal.

For zero collisionality i.e. $\bar{\nu}_{in} = 0$, (3.9) reduces to

$$\bar{\omega}_0^2 + \bar{\omega}_0 - (\bar{\omega}_{E0} + \bar{\omega}_{*0}) = 0, \tag{3.11}$$

and the equilibrium flow $\bar{\omega}_0$ is given by (Chen 1966; Jassby 1972; Gueroult *et al.* 2017)

$$\bar{\omega}_0 = \frac{-1 \pm \sqrt{1 + 4(\bar{\omega}_{E0} + \bar{\omega}_{*0})}}{2}. \tag{3.12}$$

Equation (3.12) shows that, for the equilibrium to exist at $\bar{\nu}_{in} = 0$, the following condition should be satisfied:

$$\bar{\omega}_{E0} + \bar{\omega}_{*0} > -\tfrac{1}{4}. \tag{3.13}$$

For finite collisionality, $\bar{\omega}_{E0} + \bar{\omega}_{*0} > -1/4$ is no longer required for the equilibrium to exist. From figure 2, it is seen that collisions increase the angular frequency of the fast rotation mode and decrease the angular frequency of the slow rotation mode. A more detailed discussion of collisional and non-collisional equilibrium flow can be found in Rax *et al.* (2015). Turning now to electrons and writing the equilibrium flow velocity as

$$\boldsymbol{v_{e0}} = v_{er_0}\hat{e}_r + v_{e\theta_0}\hat{e}_\theta, \tag{3.14}$$

(2.3) is solved directly to get

$$\bar{v}_{er_0} = 0; \quad \bar{v}_{e\theta_0} = \bar{r}\bar{\omega}_{0e} \quad \text{and} \quad \bar{\omega}_{0e} = \bar{\omega}_{E0} + \bar{\omega}_{*e}, \tag{3.15a–c}$$

where $\bar{\omega}_{0e}$ is the electron equilibrium flow frequency and $\bar{\omega}_{*e}$ is the electron diamagnetic drift frequency ω_{*e} normalized to the ion-cyclotron frequency, with

$$\omega_{*e} = -\frac{1}{en_0B}\frac{\boldsymbol{B} \times \boldsymbol{\nabla}(n_0T_{e0})}{rB} \cdot \hat{e}_\theta. \tag{3.16}$$

After deriving the equilibrium flow, the next section will focus on the linear stability of the plasma. Finite ion–neutral collisions (and ionization sources) result in a finite radial equilibrium flow, which adds many contributions to the dispersion relation. In the following, we will focus on the collisionless case and assume $\bar{\nu}_{in} = 0$.

https://doi.org/10.1017/S002237782300051X Published online by Cambridge University Press

4. Dispersion relation

To proceed with the derivation of the dispersion relation, we first linearize the model equations and then use the momentum equations, (2.2) and (2.3), to express the ion and electron flow in the continuity equation. The system is closed by invoking quasi-neutrality. From the electron momentum equation, (2.3), the electron flow is written in the customary form

$$\boldsymbol{v}_e = \frac{\boldsymbol{b} \times \nabla \phi}{B} + \frac{1}{en_e} \frac{\boldsymbol{b} \times \nabla (n_e T_e)}{B}. \tag{4.1}$$

When $\boldsymbol{B}$ is homogeneous and straight (linear plasma column), for any function A, we have

$$\nabla \cdot (\boldsymbol{b} \times \nabla A) = 0. \tag{4.2}$$

Therefore, on multiplying equation (4.1) with n_e and taking the divergence on both sides

$$\nabla \cdot (n_e \boldsymbol{v}_e) = \frac{\boldsymbol{b} \times \nabla \phi}{B} \cdot \nabla n_e, \tag{4.3}$$

which upon linearization yields

$$\nabla \cdot (n_e \boldsymbol{v}_e)|_1 = \frac{im}{rB}[-\phi_1 n_0' + \phi_0' n_1] \tag{4.4}$$

$$= -im\frac{\phi_1}{rB} n_0' + im\omega_{E0} n_1. \tag{4.5}$$

Combining equation (4.5) and the electron continuity equation ((2.1)), one obtains the relationship between perturbed density (n_1) and perturbed potential (ϕ_1)

$$\frac{n_1}{n_0} = \frac{m}{rL_n} \frac{1}{\omega - m\omega_{E0}} \frac{\phi_1}{B}. \tag{4.6}$$

Normalizing length to ion Larmor radius (ρ_i) and frequencies to the ion-cyclotron frequency (ω_{ci}), the normalized form of the above equation is

$$\bar{n}_1 = \frac{m}{\bar{r}\bar{L}_n} \frac{1}{\bar{\omega} - m\bar{\omega}_{E0}} \tau \bar{\phi}_1, \tag{4.7}$$

where $\tau = T_{e0_{\mathrm{ref}}}/T_{io}$ with $T_{e0_{\mathrm{ref}}}$, the reference value of the electron temperature. It should be noted that the radial variation of the electron temperature is retained here but,since the diamagnetic flux is divergence free ((4.1)–(4.3)), it does not enter the continuity equation. The relation between the perturbed density of electrons and perturbed potential given by (4.7) is therefore identical to that of Chen (1966), Rognlien (1973) and Gueroult *et al.* (2017), where the electron diamagnetic flow was neglected.

https://doi.org/10.1017/S002237782300051X Published online by Cambridge University Press

Turning now to ions, the linearized momentum equation writes

$$-\mathrm{i}\omega \boldsymbol{v}_{i1} + (\boldsymbol{v}_{i0}\cdot\nabla)\boldsymbol{v}_{i1} + (\boldsymbol{v}_{i1}\cdot\nabla)\boldsymbol{v}_{i0} = \frac{e}{m_i}[-\nabla\phi + \boldsymbol{v}_{i1}\times\boldsymbol{B}] - \frac{T_i}{m_i}\nabla\frac{n_1}{n_o}. \tag{4.8}$$

For a background rigid body rotation, $\boldsymbol{v}_{i0} = r\omega_0\hat{e}_\theta$, the inertial terms can be written as

$$(\boldsymbol{v}_{i0}\cdot\nabla)\boldsymbol{v}_{i1} = im\omega_0\boldsymbol{v}_{i1} - \omega_0\boldsymbol{v}_{i1}\times\boldsymbol{b}, \tag{4.9}$$

and

$$(\boldsymbol{v}_{i1}\cdot\nabla)\boldsymbol{v}_{i0} = v_{ir1}\frac{\partial\boldsymbol{v}_{i0}}{\partial r} + \frac{v_{i\theta 1}}{r}\frac{\partial\boldsymbol{v}_{i0}}{\partial\theta} = -\omega_0\boldsymbol{v}_{i1}\times\boldsymbol{b}. \tag{4.10}$$

When included in the linearized ion momentum equation, (4.8), it yields

$$-\mathrm{i}(\omega - m\omega_0)\boldsymbol{v}_{i1} = -\frac{\omega_{\mathrm{ci}}}{B}\nabla\phi + (\omega_{\mathrm{ci}} + 2\omega_0)\boldsymbol{v}_{i1}\times\boldsymbol{b} - \frac{\omega_{\mathrm{ci}}T_i}{eB}\nabla\frac{n_1}{n_o}. \tag{4.11}$$

The background flow enters in the Doppler shifted frequency, $\omega - m\omega_0$, on the left-hand side and in the linearized Coriolis force, $F_{\mathrm{co}} = 2m_i\boldsymbol{v}_{i1}\times\omega_0\boldsymbol{b}$, on the right-hand side.

Upon normalization, we get

$$-\mathrm{i}(\bar{\omega} - m\bar{\omega}_0)\bar{\boldsymbol{v}}_{i1} = (1 + 2\bar{\omega}_0)\bar{\boldsymbol{v}}_{i1}\times\boldsymbol{b} - \nabla\Phi_1. \tag{4.12}$$

Writing, $C = 1 + 2\bar{\omega}_0$, the factor by which the Laplace force is modified due to the inertial force, $\bar{\omega}_{\mathrm{ph}} = \bar{\omega} - m\bar{\omega}_0$, and the normalized Doppler shifted frequency and combining the perturbed density and potential terms into $\Phi_1 = \bar{n}_1 + \tau\bar{\phi}_1$, the linearized ion momentum equation then writes

$$-\mathrm{i}\bar{\omega}_{\mathrm{ph}}\bar{\boldsymbol{v}}_{i1} = -\nabla\Phi_1 + C\bar{\boldsymbol{v}}_{i1}\times\boldsymbol{b}. \tag{4.13}$$

Taking first the cross-product of (4.13) with $\boldsymbol{b}$ and using again (4.13) to replace $\boldsymbol{v}_{i1}\times\boldsymbol{b}$ in that new equation, we get

$$\bar{\boldsymbol{v}}_{i1} = \frac{C}{C^2 - \bar{\omega}_{\mathrm{ph}}^2}\left[\boldsymbol{b}\times\nabla\Phi_1 + i\frac{\bar{\omega}_{\mathrm{ph}}}{C}\nabla\Phi_1\right]. \tag{4.14}$$

The first term in the brackets is the combination of the perturbed $E\times B$ and diamagnetic flows. The second one is the polarization flow. Inertial effects are included in the factor C. The polarization flow matters when the mode frequency ω is comparable to ω_{ci}, which is precisely the regime of interest here. Note that the polarization flow makes the plasma incompressible form ($\nabla\cdot\bar{\boldsymbol{v}}_{i1} = 0$).

The final step needed before obtaining the dispersion relation is to compute the linearized divergence of the ion particle flux

$$\nabla\cdot(n_i\bar{v}_i)|_1 = n_0\nabla\cdot\bar{\boldsymbol{v}}_{i1} + \bar{\boldsymbol{v}}_{i1}\cdot\nabla n_0 + \bar{\boldsymbol{v}}_0\cdot\nabla n_1. \tag{4.15}$$

These terms are given by

$$n_0\nabla\cdot\bar{\boldsymbol{v}}_{i1} = n_0\frac{i\bar{\omega}_{\mathrm{ph}}}{C^2 - \bar{\omega}_{\mathrm{ph}}^2}\nabla^2\Phi_1, \tag{4.16}$$

$$\bar{\boldsymbol{v}}_{i1}\cdot\nabla n_0 = \frac{C}{C^2 - \bar{\omega}_{\mathrm{ph}}^2}\left[-\frac{im}{\bar{r}}\Phi_1 n_0' + i\frac{\bar{\omega}_{\mathrm{ph}}}{C}\Phi_1' n_0'\right], \tag{4.17}$$

$$\bar{\boldsymbol{v}}_0\cdot\nabla n_1 = im\bar{\omega}_0 n_1, \tag{4.18}$$

where $\nabla^2\Phi_1 = \Phi_1'' + \Phi_1'/r - m^2/r^2\Phi_1$.

https://doi.org/10.1017/S002237782300051X Published online by Cambridge University Press

Combining quasi-neutrality, $n_e = n_i$, and the continuity equations yields

$$\boldsymbol{\nabla} \cdot (n_e \boldsymbol{v}_e)|_1 = \boldsymbol{\nabla} \cdot (n_i \boldsymbol{v}_i)|_1, \tag{4.19}$$

which implies

$$\frac{m}{\bar{r}} \frac{1}{\bar{L}_n} \tau \bar{\phi}_1 + m \bar{\omega}_{E0} \bar{n}_1 = \frac{C}{C^2 - \bar{\omega}_{\rm ph}^2} \left[\frac{m}{\bar{r}} \frac{1}{\bar{L}_n} \Phi_1 - \frac{\bar{\omega}_{\rm ph}}{C} \frac{1}{\bar{L}_n} \Phi_1' + \frac{\bar{\omega}_{\rm ph}}{C} \nabla^2 \Phi_1 \right] + m \bar{\omega}_0 \bar{n}_1. \tag{4.20}$$

Now, using the electron continuity equation, (4.7), to express $\bar{n}_1$ as a function of $\bar{\phi}_1$ in $\Phi_1 = \bar{n}_1 + \tau \bar{\phi}_1$, we get

$$\Phi_1 = (1 + \alpha_*) \tau \bar{\phi}_1, \tag{4.21}$$

with

$$\alpha_* = - \frac{m \bar{\omega}_{*0}}{\bar{\omega}_{\rm ph} - m(\bar{\omega}_{E0} - \bar{\omega}_0)}. \tag{4.22}$$

Note that, when the ion pressure gradient is neglected in the ion momentum equation ($T_i = 0$), we get $\alpha_* = 0$ and $\Phi_1 = \tau \bar{\phi}_1$.

Using (4.21) to express $\tau \bar{\phi}_1$ and $\bar{n}_1$ as a function of Φ_1 and recalling that, from the equation dictating the equilibrium flow, $\bar{\omega}_0 + \bar{\omega}_0^2 = \bar{\omega}_{*0} + \bar{\omega}_{E0}$, (4.20) can be written as

$$\Phi_1'' + \left[\frac{1}{\bar{r}} - \frac{1}{\bar{L}_n} \right] \Phi_1' - \frac{m^2}{\bar{r}^2} \Phi_1 + \frac{1}{\bar{r} \bar{L}_n} N \Phi_1 = 0, \tag{4.23}$$

where

$$N = m \left[\frac{C}{\bar{\omega}_{\rm ph}} - \frac{C^2 - \bar{\omega}_{\rm ph}^2}{\bar{\omega}_{\rm ph} - m \bar{\omega}_0^2} \right]. \tag{4.24}$$

Equations (4.23) and (4.24) provide an extension of the model derived in Chen (1966) for arbitrary frequency values but in the limit of vanishing gyro-viscosity. The low-frequency expansion involved in Chen (1966) consists in approximating $C^2 - \bar{\omega}_{\rm ph}^2 \sim C^2$. In this limit

$$N = m \left[\frac{C}{\bar{\omega}_{\rm ph}} - \frac{C^2}{\bar{\omega}_{\rm ph} - m \bar{\omega}_0^2} \right], \tag{4.25}$$

and one exactly recovers (25) in Chen (1966) for $\boldsymbol{\nabla} \cdot \boldsymbol{\pi}_i = 0$.

Note that N is radially constant because of the assumption of rigid body rotation. The differential equation (4.23) can be solved by the method used in Rosenbluth *et al.* (1962), Chen (1966) and Rognlien (1973) by exploiting the change of variables

$$z = r^2 / r_0^2, \tag{4.26}$$

where r_0 is the width of the Gaussian used to parametrize the density profile defined by (2.6*a*,*b*), and enters (4.23) through $1/L_n = 2r/r_0^2$, combined with

$$\Phi_1 = z^{-1/2} \, {\rm e}^{z/2} W(z), \tag{4.27}$$

to obtain Whittaker's equation (Whittaker & Watson 1966)

$$\frac{{\rm d}^2 W}{{\rm d}z^2} + \left\{ -\frac{1}{4} + \frac{N+1}{2z} + \frac{1 - m^2}{4z^2} \right\} W = 0. \tag{4.28}$$

https://doi.org/10.1017/S002237782300051X Published online by Cambridge University Press

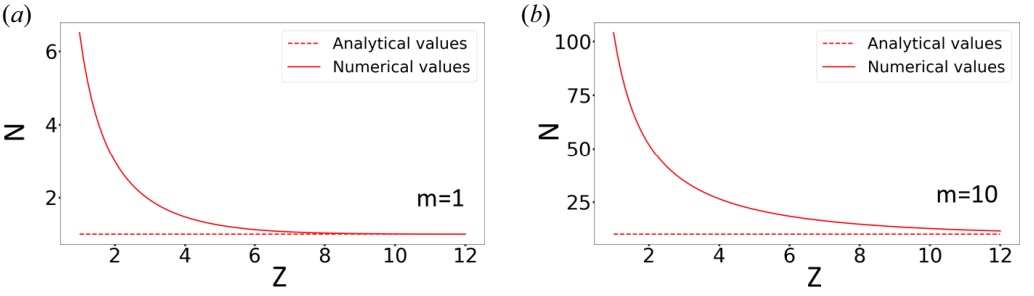

FIGURE 3. Values of N corresponding to the first zero of Kummer's function for different values of $Z = r_b^2/r_0^2$. The solid line denotes the values evaluated numerically and the dashed line (−−) denotes the asymptotic values.

The non-singular solution of this equation is given by,

$$W_{N,m}(z) = z^{(m+1)/2}\,\mathrm{e}^{-z/2} F\left(\frac{m-N}{2}, 1+2m; z\right), \tag{4.29}$$

where $F((m-N)/2, 1+2m; z)$ is the confluent hyper-geometric function of the first kind known as Kummer's function. Imposing the boundary condition $\Phi(Z) = 0$, with $Z = r_b^2/r_0^2$ (where r_b is the outer radial boundary of the cylindrical vessel), fully determines the possible values of N, which for different mode numbers m are evaluated from the zeros of the Kummer function $F((m-N)/2, 1+2m; Z)$. These zeros can be evaluated numerically. Alternatively, the asymptotic values of N ($Z \to \infty$) are $N = m + 2n$, where $n = 0, 1, 2, 3, \ldots$ is the radial mode number (Rosenbluth *et al.* 1962; Chen 1966). The radial mode number n simply indicates which zero of F we are referring to; e.g. $n = 0$ implies the first value of N at which the function F goes to zero, $n = 1$ implies the second value of N at which the function F goes to zero and so on. In figure 3, the numerical solutions for N, obtained using the whitm function in the Python library mpmath, are compared with the asymptotic solutions for $n = 0$. Convergence is reached at $Z > 6$ for $m = 1$, but higher Z values are required at high m. For practical applications, such as in MISTRAL where $r_b = 10$cm and $r_0 \approx 3$ cm, it is, therefore, preferable to use the numerical solution. In the following discussion, we will only use the values of N evaluated numerically.

Note that, for a given radial mode number n, the value of N and the eigenfunction shape only depend on the azimuthal mode number m and the value of Z, which represents the ratio of the cylinder radius to the plasma radius. The eigenfunctions are therefore independent of the background flow $\bar{\omega}_0$. Eigenfunctions obtained for $m = 1, 2, 5$ and 10 for different Z values, including the one of MISTRAL ($Z \approx 10.8$), are shown in figure 4. The solutions of (4.24) are purely real, therefore, there is no radial variation of the phase of the eigenfunctions.

Once N is known, rearranging (4.24) gives the cubic dispersion relation

$$\bar{\omega}_{\mathrm{ph}}^3 - \frac{N}{m}\bar{\omega}_{\mathrm{ph}}^2 + (N\bar{\omega}_0^2 - 2C\bar{\omega}_0)\bar{\omega}_{\mathrm{ph}} - mC\bar{\omega}_0^2 = 0, \tag{4.30}$$

from which the mode growth rate and frequency can be computed.

https://doi.org/10.1017/S002237782300051X Published online by Cambridge University Press

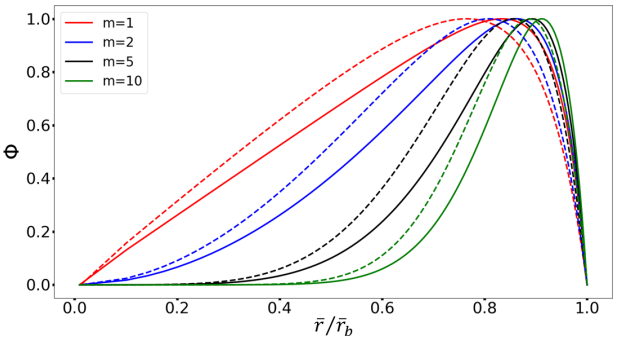

FIGURE 4. Eigenfunction Φ as a function of $\bar{r}/\bar{r}_b$ for $m = 1, 2, 5$ and 10. The solid lines represent the case when $Z = 10.8$ (for MISTRAL) and the dashed lines represent the case when $Z = 6.9$.

If the LFA is applied i.e. if $C^2 - \bar{\omega}_{\rm ph}^2 \approx C^2$, the equation above becomes

$$\frac{N}{m}\bar{\omega}_{\rm ph}^2 - (N\bar{\omega}_0^2 - 2C\bar{\omega}_0)\bar{\omega}_{\rm ph} + mC\bar{\omega}_0^2 = 0, \tag{4.31}$$

which is exactly equivalent to (30) in Chen (1966) if the terms with $1/r_0^2$ entering because of the gyro-viscosity tensor are dropped.

4.1. *Local limit*

To make the link with previous work, e.g. Chen (1966) and Gueroult *et al.* (2017), the local limit is obtained by assuming $\Phi_1' = 0$, $\Phi_1'' = 0$ in (4.23)

$$\bar{\omega}_{\rm ph}^3 - \frac{m\bar{r}_0^2}{2\bar{r}^2}\bar{\omega}_{\rm ph}^2 + \left(-2C\bar{\omega}_0 + m^2\bar{\omega}_0^2\frac{\bar{r}_0^2}{2\bar{r}^2}\right)\bar{\omega}_{\rm ph} - mC\bar{\omega}_0^2 = 0. \tag{4.32}$$

This is the same as the dispersion relation obtained by equating (17*a*) and (17*b*) in Gueroult *et al.* (2017). Note that, in Gueroult *et al.* (2017), the diamagnetic drift of the ions was neglected. It is kept here but only enters the equation by modifying the equilibrium azimuthal flow $\bar{\omega}_0$. Various asymptotic regimes and stability limits regarding the dispersion relation ((4.32)) have been discussed in Gueroult *et al.* (2017) for $-0.25 \leq \omega_{E0} \leq 0$. We extend this discussion to $-0.5 \leq \omega_0 \leq 1.5$ in § 5.

Using the LFA in (4.32), leads to the following dispersion relation:

$$\bar{\omega}_{\rm ph}^2 + \left(\frac{4\bar{r}^2C\bar{\omega}_0}{m\bar{r}_0^2} - m\bar{\omega}_0^2\right)\bar{\omega}_{\rm ph} + \frac{2\bar{r}^2C\bar{\omega}_0^2}{\bar{r}_0^2} = 0. \tag{4.33}$$

5. Linear stability

In this section, the linear stability and the parametric dependency of the growth rate are discussed for the global dispersion relation derived in § 4. We first examine the role of the radial mode number n in linear stability.

Figure 5 represents the radial mode number n which yields the largest growth rate evaluated using the global dispersion relation ((4.30)) for a given mode number m as a function of Z and $\omega_0/\omega_{\rm ci}$. For $m = 1, 2$ and for the given range of $\omega_0/\omega_{\rm ci}$, the radial mode number $n = 0$ has the largest growth rate for $Z < 3$. For $Z > 3$, higher radial mode numbers are progressively dominant as $\bar{\omega}_0$ and Z increases. For $m = 10$, the lowest radial

https://doi.org/10.1017/S002237782300051X Published online by Cambridge University Press

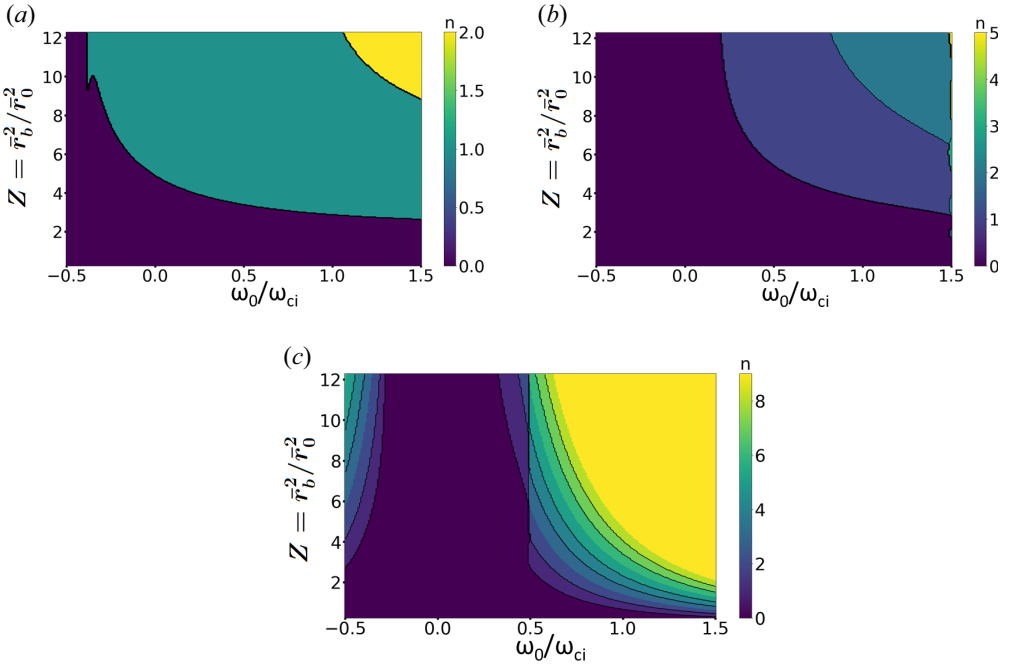

FIGURE 5. Radial mode number n corresponding to the largest growth rate $\bar{\gamma}$ as a function of $Z = \bar{r}_b^2/\bar{r}_0^2$ and ω_0/ω_{ci}. The colour bar represents the radial mode number n.

mode number $n = 0$ corresponds to the largest growth rate when $-0.3 \leq \omega_0/\omega_{ci} \leq 0.3$. For large values of $|\bar{\omega}_0|$, the radial mode number n that gives the largest growth rate also increases with $|\bar{\omega}_0|$ and Z. When the growth rate is evaluated using the global dispersion relation with LFA ((4.31)), the lowest radial mode number $n = 0$ has the largest growth rate. In the following discussion, we will focus on the radial mode number, $n = 0$.

The most unstable mode obtained from the global dispersion relation without ((4.30)) and with LFA ((4.31)) for mode number $n = 0$ and $m = 1$, 2and10 is shown in figure 6 as a function of ω_0/ω_{ci} and Z. The two models predict the growth rate to increase with $|\bar{\omega}_0|$, with an asymmetry with respect to $\bar{\omega}_0$, originating from the inertial term in the effective magnetization factor C. The difference between two models increases with increasing m and equilibrium flow frequency $\bar{\omega}_0$. For $m = 10$, the region of higher growth rate, as well as the stability region, are radically different with and without LFA. Without the LFA, the largest growth rate is obtained at low Z and large $\bar{\omega}_0$, whereas this becomes a stable region and the growth rate is maximum at large Z with the LFA. The difference in the stability region stems from the neglect of the terms of the order of $\bar{\omega}_{ph}^3$. For frequencies satisfying $\omega - m\omega_0 \ll \omega_{ci}$, the LFA is valid, and hence the dispersion relation with LFA ((4.31)) yields correct results, but as we move towards regimes with high-frequency values, the LFA ordering fails. There is a common region that is stable ($\bar{\gamma} = 0$) for both the cases and that region corresponds to $\bar{\omega}_0 = 0$.

5.1. *Effect of LFA*

The validity domain of the LFA as a function of ω_0/ω_{ci} is emphasized in figure 7, where the solution without the LFA ((4.30)) with the red curve, is compared with the solution with the LFA valid when $\omega_{ph}/\omega_{ci} = O(\rho^2)$ (green curve, (4.31)) and to another solution

https://doi.org/10.1017/S002237782300051X Published online by Cambridge University Press

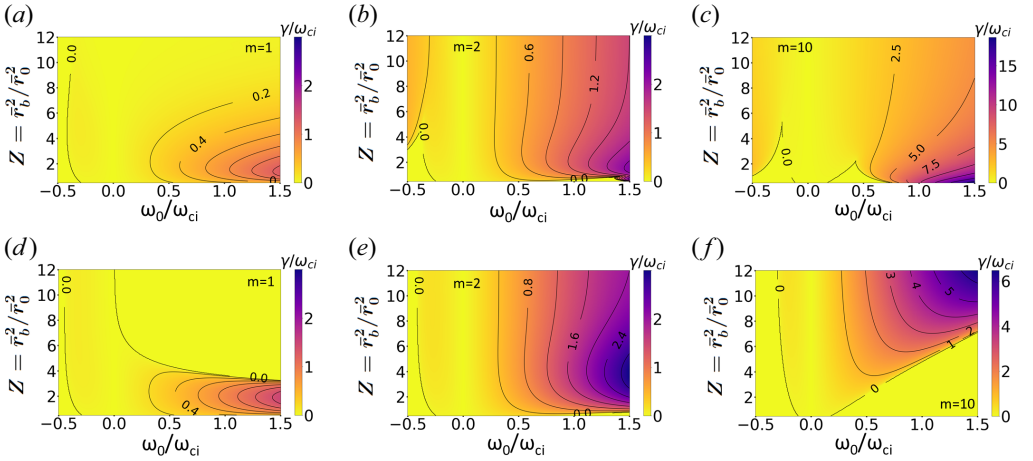

FIGURE 6. Normalized growth rate γ/ω_{ci} as a function of normalized equilibrium flow frequency (ω_0/ω_{ci}) and $Z = \bar{r}_b^2/\bar{r}_0^2$, where $\bar{r}_b$ is the radial boundary and $\bar{r}_0$ is the width of the Gaussian normalized to the Larmor radius ρ_i for the global dispersion relation given by (4.30) (*a–c*) and (4.31) (*d–f*). The colour bar represents the normalized growth rate ($\bar{\gamma} = \gamma/\omega_{ci}$).

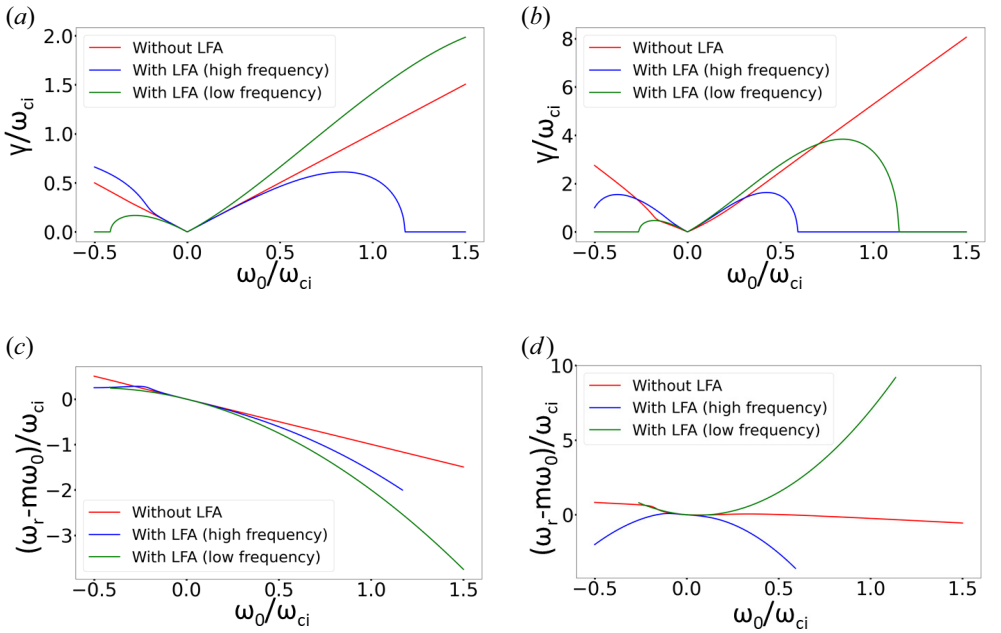

FIGURE 7. Normalized growth rate γ/ω_{ci} and normalized Doppler shifted frequency $(\omega_r - m\omega_0)/\omega_{ci}$ as a function of normalized equilibrium flow frequency (ω_0/ω_{ci}) for (*a*,*c*) $m = 2$ and (*b*,*d*) $m = 20$ for $Z = 10.78$.

with the LFA but valid at higher frequency i.e. $\omega_{ph}/\omega_{ci} = O(\rho)$ (blue curve, (38) in Chen (1966) with $\nabla \cdot \boldsymbol{\pi}_i = 0$).

All three dispersion relations predict the same growth rate $\bar{\gamma}$ and the real part of Doppler shifted frequency $\bar{\omega}_r - m\bar{\omega}_0$ when the values of $\bar{\omega}_0$ are close to zero. As $\bar{\omega}_0$ increases, the model predictions deviate, especially for higher mode numbers. This accounts from

https://doi.org/10.1017/S002237782300051X Published online by Cambridge University Press

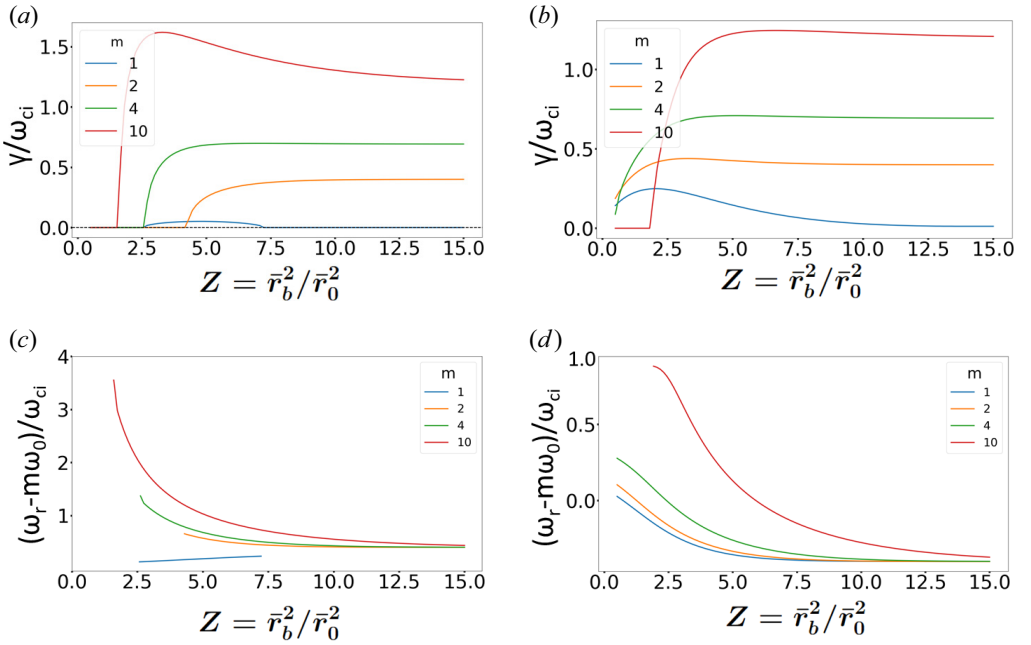

FIGURE 8. Normalized growth rate $\bar{\gamma} = \gamma/\omega_{ci}$ and normalized Doppler shifted frequency $(\omega_r - m\omega_0)/\omega_{ci}$ as a function of $Z = \bar{r}_b^2/\bar{r}_0^2$ for various mode numbers m using dispersion relation ((4.30)); (*a*,*c*) for $\bar{\omega}_0 = -0.4$ and (*b*,*d*) for $\bar{\omega}_0 = 0.4$.

the fact that terms involving higher orders of $\bar{\omega}_{ph} = \bar{\omega} - m\bar{\omega}_0$, i.e. the Doppler shifted frequency, have been neglected in evaluating the dispersion relations in Chen (1966) and as the factor $m\bar{\omega}_0$ increases, the assumption is no longer valid.

5.2. *Impact of radial boundary on growth rate*

The position of the boundary also has a strong influence on the mode growth rate for a given value of $\bar{\omega}_0$. The growth rate and real part of the Doppler shifted frequency at different radial boundary positions $\bar{r}_b$ keeping $\bar{r}_0$ fixed, for various values of m evaluated by the global dispersion relation ((4.30)) areshown in figure 8. At fixed plasma size, $\bar{r}_0$, increasing the cylinder radius $\bar{r}_b$, for which $\Phi(Z) = 0$ is imposed, first destabilizes all modes and then has limited-to-no impact on the growth rate once $\bar{r}_b \sim 3\bar{r}_0$ ($Z \sim 9$). Note that $m = 1$ has a different behaviour and gets fully stabilized when the bounding cylinder radius is increased.

For the real part of the normalized Doppler shifted frequency $\bar{\omega}_r - m\bar{\omega}_0$, for all mode numbers, the frequency is maximum for small values of Z and then decreases as Z increases except for $m = 1$ when $\bar{\omega}_0 = -0.4$. The sign of $\bar{\omega}_0$ plays a critical role in determining the sign of Doppler shifted frequency $(\bar{\omega}_r - m\bar{\omega}_0)$.

5.3. *Eigenfunction and phase difference*

The expression of the eigenfunctions for the normalized perturbed density n_1/n_0 and perturbed potential $e\phi_1/T_{e0_{ref}}$ is obtained by using (4.7) and (4.21)

$$\bar{n}_1 = \frac{m}{\bar{r}\bar{L}_n(\bar{\omega} - m\bar{\omega}_{E0})}\frac{\Phi_1}{(1+\alpha_*)}, \tag{5.1}$$

https://doi.org/10.1017/S002237782300051X Published online by Cambridge University Press

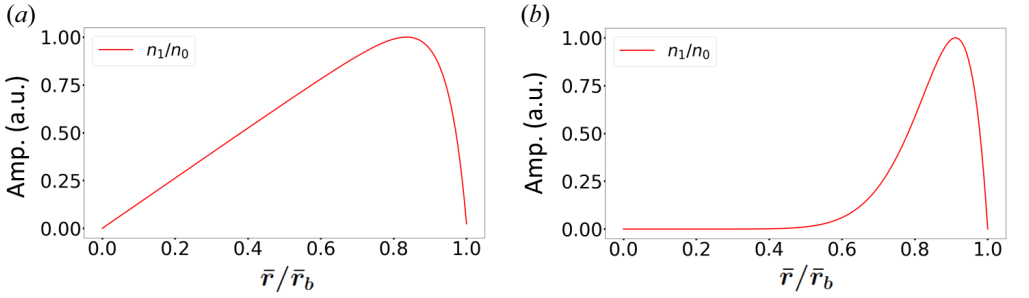

FIGURE 9. Normalized perturbed density n_1/n_0 for (*a*) $m = 1$ and (*b*) $m = 10$ as a function $\bar{r}/\bar{r}_b$ using $Z = 10.8$. The parameters used to obtain these eigenfunctions are $\bar{\omega}_{E0} = 0.95$, $\bar{\omega}_{*0} = -0.35$, $\bar{\omega}_0 = 0.42$ and $\tau = 1$.

$$\bar{\phi}_1 = \frac{\Phi_1}{(1 + \alpha_*)\tau}, \tag{5.2}$$

where α_* is given by (4.22). Using these expressions, the eigenfunctions $\bar{n}_1$ for $m = 1$ and 10 are shown in figure 9 for $\tau = 1$. The perturbations in density and potential are more spread out for $m = 1$ than for $m = 10$ or, in other words, modes with higher azimuthal mode numbers are more localized towards the boundary region, as already discussed in figure 4.

Another essential information regarding the mode structure of the instability is the phase difference between density and potential fluctuations. This is a quantity that can be measured experimentally and which determines the level of particle flux driven by the fluctuations $\bar{n}_1\bar{\boldsymbol{v}}_{i1}$. To calculate the phase difference between $\bar{\phi}_1$ and $\bar{n}_1$, we divide (5.2) by (5.1)

$$\frac{\bar{\phi}_1}{\bar{n}_1} = (\bar{\omega} - m\bar{\omega}_{E0})\frac{\bar{r}\bar{L}_n}{m\tau}. \tag{5.3}$$

Writing $\bar{\phi}_1/\bar{n}_1 = A\,\mathrm{e}^{\mathrm{i}\phi_p}$, the phase difference ϕ_p is,

$$\phi_p = \tan^{-1}\left(\frac{\bar{\gamma}}{\bar{\omega}_r - m\bar{\omega}_{E0}}\right). \tag{5.4}$$

Figure 10 shows the phase difference between $\bar{\phi}_1$ and $\bar{n}_1$ as a function of $\omega_{E0}/\omega_{\mathrm{ci}}$ and $-2/\bar{r}_0^2$ for $m = 1$ and $m = 2$ with $\tau = 1$. Note that $\bar{r}_0$ does not appear explicitly in (5.4) but comes in the expression for $Z = \bar{r}_b^2/\bar{r}_0^2$ and $\bar{\omega}_0$ which determines $\bar{\gamma}$ and $\bar{\omega}_r$. Therefore, by varying $\bar{r}_0$, the combined effect of Z as well as $\bar{\omega}_0$ on the phase difference can be observed. The phase shift is close to zero, except in a narrow region where $\bar{\omega}_r - m\bar{\omega}_{E0}$ is approaching zero. In this region, the phase shift becomes large, $|\phi_p| \sim 90^\circ$ and changes sign. Furthermore, the critical value of $\bar{\omega}_{E0}$ at which the phase shift changes from negative to positive increases with decreasing $\bar{r}_0$.

5.4. *Azimuthal mode number spectra*

In figure 11, the normalized growth rate $\bar{\gamma}$ and normalized real frequency $\bar{\omega}_r$, computed numerically by solving the dispersion relation ((4.30)) are shown as a function of m. The growth rate is increasing with the mode number m irrespective of the sign of $\bar{\omega}_0$. At high m, finite Larmor radius (FLR) effects are strongly stabilizing (Hoh 1963) and should be taken into account. In a fluid description they enter in the gyroviscosity tensor, neglected

https://doi.org/10.1017/S002237782300051X Published online by Cambridge University Press

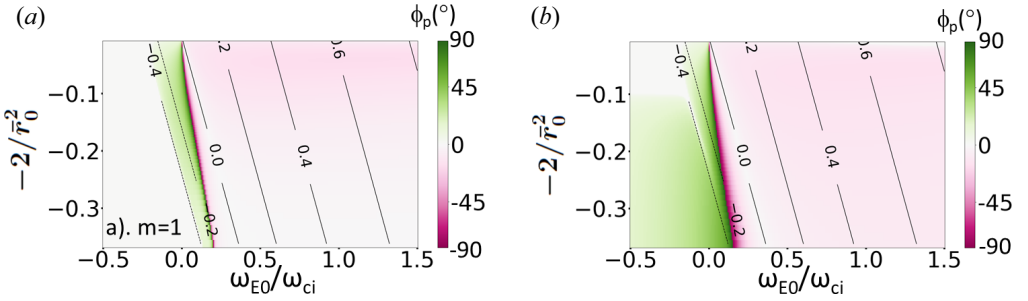

FIGURE 10. Phase difference between $\bar{\phi}_1$ and $\bar{n}_1$ for (*a*) $m = 1$ and (*b*) $m = 2$ as a function of normalized $E \times B$ flow frequency (ω_{E0}/ω_{ci}) and $-2/\bar{r}_0^2$, where $\bar{r}_0$ is the normalized plasma size. The colour bar represents the phase difference in degrees and the constant lines on the contour represent $\bar{\omega}_0$.

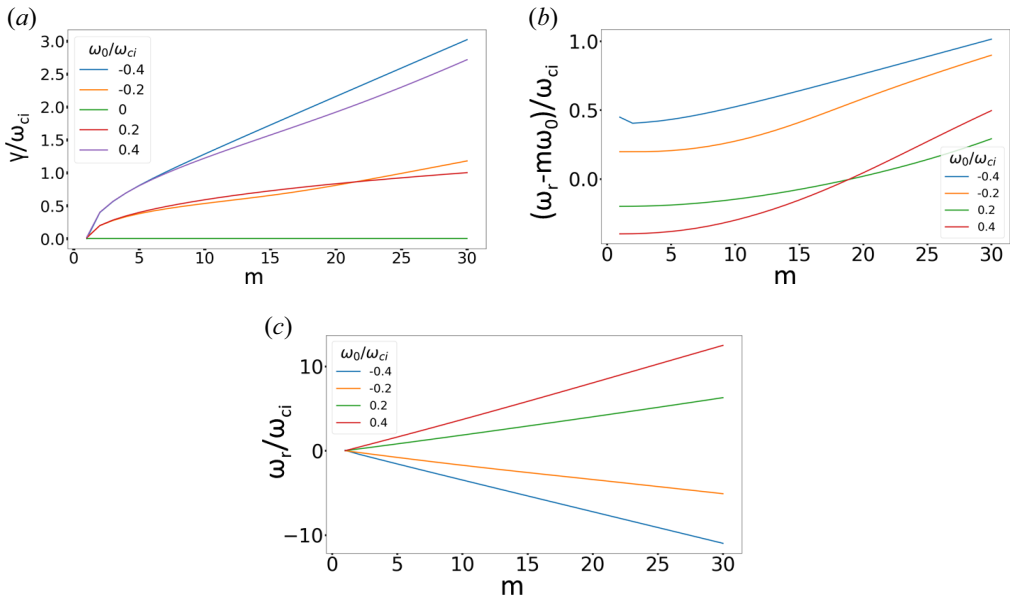

FIGURE 11. (*a*) Normalized growth rate $\bar{\gamma} = \gamma/\omega_{ci}$, (*b*) normalized Doppler shifted frequency $(\omega_r - m\omega_0)/\omega_{ci}$ and (*c*) normalized frequency $\bar{\omega}_r = \omega_r/\omega_{ci}$ as a function of azimuthal mode number m for various values of normalized equilibrium flow frequency $\bar{\omega}_0 = \omega_0/\omega_{ci}$ used in the global dispersion relation ((4.30)).

here, but have been shown to stabilize high m numbers in Chen (1966). In other words, FLR effects are important when $k_\theta \rho_i \sim 1$ where $k_\theta = m/r$ is the azimuthal wavenumber. This corresponds to, $m \sim r/\rho_i$, which implies that the FLR stabilization ($\gamma \to 0$) comes into effect when $m > r/\rho_i$.

The growth rate is zero for $\bar{\omega}_0 = 0$, which is consistent with the linear stability diagram (figure 6). For $m = 1$, $\bar{\gamma}$ is of the order of $10^{-2}\omega_{ci}$ for positive values of $\bar{\omega}_0$ and for $\bar{\omega}_0 = -0.2$, and zero for $\bar{\omega}_0 = -0.4$ and 0. For similar values of $\bar{\omega}_0$ but in opposite directions there is a small difference in the growth rate up to $m = 5$ and this difference in the growth rate escalates with increasing mode number m. Overall, the growth rate increases with the increase in $\bar{\omega}_0$. The Doppler shifted frequency $(\bar{\omega}_r - m\bar{\omega}_0)$ has the sign opposite to that of

https://doi.org/10.1017/S002237782300051X Published online by Cambridge University Press

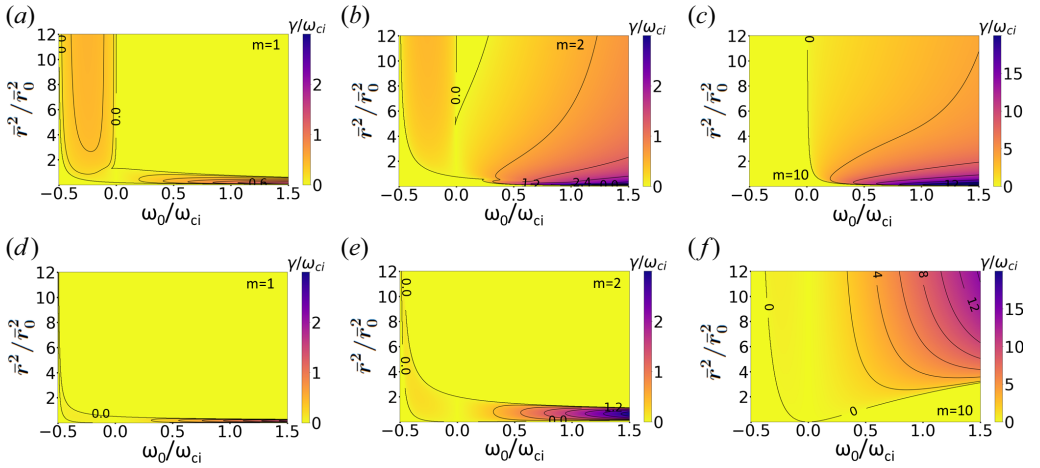

FIGURE 12. Normalized growth rate γ/ω_{ci} as a function of normalized equilibrium flow frequency (ω_0/ω_{ci}) and $\bar{r}^2/\bar{r}_0^2$ for the local dispersion relation given by (4.32) (*a–c*) and (4.33) (*d–f*). The colour bar represents the normalized growth rate ($\bar{\gamma} = \gamma/\omega_{ci}$).

$\bar{\omega}_0$ for $\bar{\omega}_0 < 0$. For $\bar{\omega}_0 > 0$, the Doppler shifted frequency has the sign opposite to $\bar{\omega}_0$ until $m < 20$. The real part of the frequency $\bar{\omega}_r$ has also been shown in figure 11(*c*) to show the dominance of the factor $m\bar{\omega}_0$.

6. Comparison of local and global dispersion relations

In this section, the impact of the local approximation ((4.32) and (4.33)) is discussed. In figure 12, the mode growth rate obtained in the local approximation with and without LFA is shown as a function of $\bar{\omega}_0$ and $\bar{r}^2/\bar{r}_0^2$ for $m = 1, 2$ and 10. Similarly to the radially global results, the LFA assumption is shown to have a validity domain restricted to low $\bar{\omega}_0$ values and low m. Relaxing the LFA opens up new instability regions, in particular at low m, where an unstable zone is obtained at $\bar{\omega}_0 < 0$. For $\bar{\omega}_0 = 0$, no instability exists and stable anti-drift modes with a propagation frequency $\bar{\omega}_r = m\bar{r}_0^2/2\bar{r}^2$ are predicted without the LFA (Fridman 1964).

In contrast to the local dispersion relation, which evaluates the growth rate at each radial position, the global dispersion relation describes the growth rate of an eigenmode extending over the whole cylinder radius. To compare the local and global model predictions, we show in figure 13, the maximum growth rate, $\bar{\gamma}_{\max}$, obtained with the local model over the interval $0 \leq \bar{r} \leq \bar{r}_b$ as a function of $\bar{\omega}_0$ and $Z = \bar{r}_b^2/\bar{r}_0^2$. This quantity is compared with the global model predictions in figure 13(*d–f*). All results are shown without the LFA. In figure 13(*a–c*), we see that, for $\bar{\omega}_0 > 0$, the value of $\bar{\gamma}_{\max}$ is largely independent of $Z = \bar{r}_b^2/\bar{r}_0^2$. This is because the radial position at which the maximum growth rate is obtained in the local model is close to zero, see figure 12(*a–c*). The situation is different for $\bar{\omega}_0 < 0$ and low m, where the local growth rate increases with $\bar{r}$ (see figure 12*a*). This is reflected by an increase of $\bar{\gamma}_{\max}$ with $\bar{r}_b^2/\bar{r}_0^2$.

In both cases, $\bar{\gamma}_{\max}$ is obtained close to the radial boundaries, either $\bar{r} = 0$ or $\bar{r} = \bar{r}_b$, where global effects are non-negligible. This is why the relative difference between the $\bar{\gamma}_{\max}$ and $\bar{\gamma}_{\text{global}}$, shown in figure 13, is always significant, except perhaps when the growth rate is closer to zero. The dark blue region in figure 13(*d–f*) where $\bar{\gamma}_{\text{rel}}$ is maximum, corresponds to the region where $\bar{\gamma}_{\max} = 0$ but $\bar{\gamma}_{\text{global}}$ remains finite, leading to large value of $\bar{\gamma}_{\max} - \bar{\gamma}_{\text{global}}$. The white region in figure 13(*d–f*) corresponds to the region where both

https://doi.org/10.1017/S002237782300051X Published online by Cambridge University Press

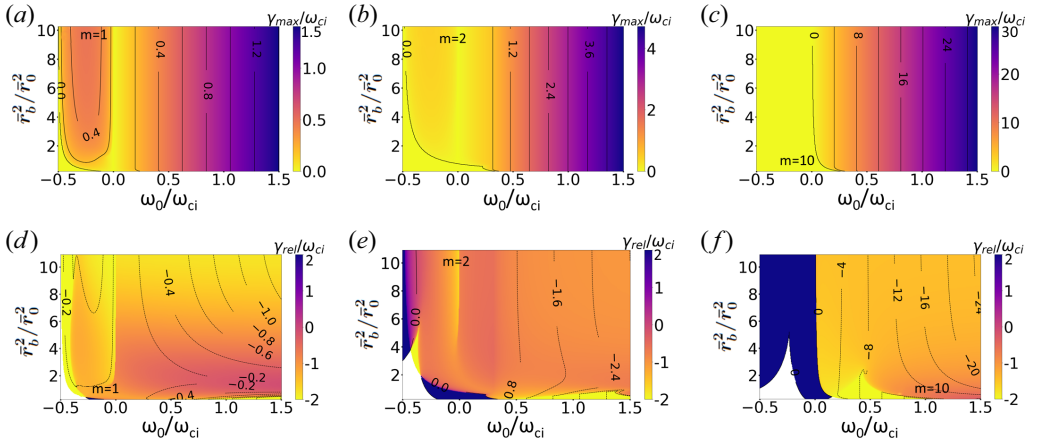

FIGURE 13. Normalized maximum growth rate $\gamma_{\max}/\omega_{\mathrm{ci}}$ as a function of normalized equilibrium flow frequency $(\omega_0/\omega_{\mathrm{ci}})$ and $\bar{r}_b^2/\bar{r}_0^2$ for the local dispersion relation given by (4.32) (*a–c*). Normalized relative growth rate $\gamma_{\mathrm{rel}}/\omega_{\mathrm{ci}}$ as a function of normalized equilibrium flow frequency $(\omega_0/\omega_{\mathrm{ci}})$ and $\bar{r}^2/\bar{r}_0^2$, where $\bar{\gamma}_{\mathrm{rel}} = 2(\bar{\gamma}_{\max} - \bar{\gamma}_{\mathrm{global}})/(\bar{\gamma}_{\max} + \bar{\gamma}_{\mathrm{global}})$ and $\bar{\gamma}_{\mathrm{global}}$ is evaluated using (4.30) (*d–f*). The constant lines on (*d–f*) represents the difference between $\bar{\gamma}_{\max}$ and $\bar{\gamma}_{\mathrm{global}}$.

$\bar{\gamma}_{\max}$ and $\bar{\gamma}_{\mathrm{global}}$ correspond to zero. From the comparison, it is evident that the local dispersion relation cannot be used to study the global behaviour of weakly magnetized rotating plasma systems having frequencies comparable to the ion-cyclotron frequency.

7. Conclusions and summary

A dispersion relation for a rigid body rotating plasma in a cylindrical geometry has been derived for the radially local and global eigenmodes. The instability's growth rate is strongly dependent on the equilibrium azimuthal flow $\bar{\omega}_0$, which in turn depends on the $E \times B$ flow and the diamagnetic flow. No instability is predicted for $\bar{\omega}_0 = 0$. For fixed $\bar{\omega}_0$ and density gradient, the azimuthal mode number m and the radial boundary limit $\bar{r}_b$ are the dominant factors affecting the growth rate.

The comparison of the dispersion relation with and without LFA revealed that, as soon as the equilibrium flow frequency is a fraction of the ion-cyclotron frequency, with the exact threshold depending on the parameters m and Z, relaxing the LFA is mandatory. More precisely, the LFA becomes inaccurate when the Doppler shifted frequency, $\omega_r - m\omega_0$, becomes comparable to ω_{ci}.

The local solution of the dispersion relation was compared with the global solution (see figure 13), showing that there is no parameter range where the local model is applicable. This is because the local model predicts a maximum growth rate either close to the plasma axis or the outer cylinder, where boundary effects are essential. Rotating plasmas subject to centrifugal instability, as in MISTRAL, require a non-local treatment taking the boundary into account.

This work is a part of an effort aimed at developing a comprehensive theory for the description of strongly rotating weakly magnetized plasma columns. We have focused here on the collisionless case and neglected FLR effects. These assumptions will need to be relaxed and this is why we have so far refrained from making a direct comparison with MISTRAL. In particular, it has been shown in Pierre (2016) that ion–neutral collisions are important to discuss the stability mechanism of weakly magnetized rotating plasma

https://doi.org/10.1017/S002237782300051X Published online by Cambridge University Press

columns. Furthermore, shear effects which give rise to Kelvin–Helmholtz instability (Jassby 1972; Gravier *et al.* 2004; Brochard, Gravier & Bonhomme 2005) and which are important for rotating plasmas are not included in the current discussion through the assumption of rigid body rotation ($\partial\omega_0/\partial r = 0$) in the two-fluid formalism. Efforts to resolve these issues are in progress.

Acknowledgements

Views and opinions expressed are, however, those of the author(s) only and do not necessarily reflect those of the European Union or the European Commission. Neither the European Union nor the European Commission can be held responsible for them.

Editor Paolo Ricci thanks the referees for their advice in evaluating this article.

Declaration of interest

The authors report no conflict of interest.

Funding

This work has been carried out within the framework of the EUROfusion Consortium, funded by the European Union via the Euratom Research and Training Programme (Grant Agreement No 101052200 – EUROfusion).

Appendix. Typical equilibrium profile measured in the MISTRAL experiment

The experimental set-up of MISTRAL is shown in figure 14 with a comprehensive description given in Jaeger (2010), Matsukuma *et al.* (2003) and Escarguel (2010). The plasma is produced in the magnetized cylindrical column after the interaction of energetic electrons with neutrals. These energetic electrons are produced by thermionic emission in the source chamber. A polarizable grid called the separating grid is inserted at the entrance section of the linear plasma column and separates the source chamber from the linear column. Another polarizable grid called the collector is placed at the end of the plasma column.

The time-averaged electron density and plasma potential are measured with a radially movable Langmuir probe. The electron density and plasma potential profiles are shown in figures 15(*a*) and 15(*b*), for a configuration where the separating grid and collector are connected and at the negative potential. The gas used is argon and the cylinder is grounded. The magnetic field and the pressure values are $B = 16$ mT and $P = 3.6 \times 10^{-4}$ mbar, respectively.

Within the uncertainties on the measurements, the shape of the number density n_0 is Gaussian (figure 15*a*) and the plasma potential ϕ_0 is parabolic (figure 15*b*), consistent with the rigid body rotation assumption used in the model.

Table 2 gives the value of dimensionless parameters entering in the model for the MISTRAL plasma shown in figures 15(*a*) and 15(*b*).

The ion-cyclotron frequency is only a few kHz and comparable to the azimuthal flow frequency. Models valid in the low rotation regime are therefore not applicable to MISTRAL plasmas. Note that the ion–neutral collision frequency is also comparable to the ion-cyclotron frequency and the present model will need to be extended to be applicable to MISTRAL plasmas.

https://doi.org/10.1017/S002237782300051X Published online by Cambridge University Press

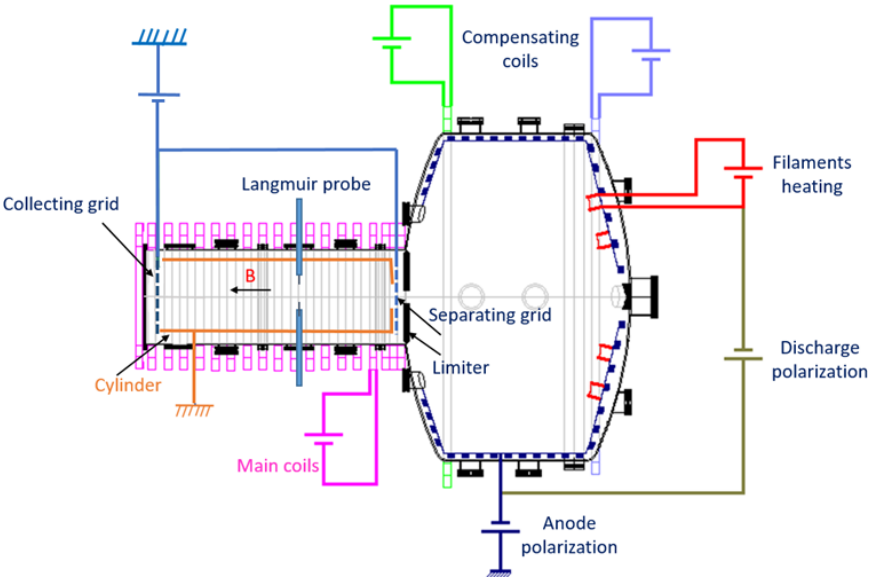

FIGURE 14. Electrical schematic of MISTRAL. In the source chamber, 32 filaments randomly emit energetic primary electrons, which are then injected into the argon-filled cylindrical chamber. A magnetic plasma column is produced by the interaction of these primary electrons moving along the magnetic field.

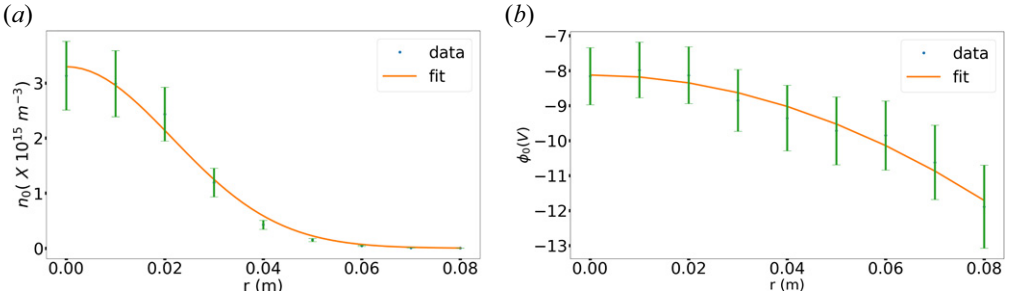

FIGURE 15. (*a*) Radial profile of electron number density n_0 for argon plasma with Gaussian fit. (*b*) Radial profile of plasma potential ϕ_0 for argon plasma with parabolic fit.

Parameter	Unit	Magnitude
Ion-cyclotron frequency $\omega_{ci}/2\pi$	KHz	6.1
Ion Larmor radius ρ_i	cm	1.28
Normalized ExB drift frequency ω_{E0}/ω_{ci}	—	−1.8
Normalized diamagnetic drift frequency ω_{*0}/ω_{ci}	—	−0.4
Normalized ion–neutral collision frequency ν_{in}/ω_{ci}	—	0.4
Equilibrium flow frequency ω_0/ω_{ci}	—	−0.4
Plasma radius r_0	cm	0.3
Normalized density gradient scale length ρ_i/L_n (at $r = 2.5$ cm)	—	0.7
$Z = r_b^2/r_0^2$	—	10.8

TABLE 2. Various parameters in MISTRAL for *Ar* at $B = 16$ mT.

https://doi.org/10.1017/S002237782300051X Published online by Cambridge University Press

REFERENCES

ABOLMASOV, S.N. 2012 Physics and engineering of crossed-field discharge devices. *Plasma Sources Sci. Technol*. **21** (3), 035006.

ANNARATONE, B.M., ESCARGUEL, A., LEFEVRE, T., REBONT, C., CLAIRE, N. & DOVEIL, F. 2011 Rotation of a magnetized plasma. *Phys. Plasmas* **18**, 032108.

BROCHARD, F., GRAVIER, E. & BONHOMME, G. 2005 Transition from flute modes to drift waves in a magnetized plasma column. *Phys. Plasmas* **12** (6).

CHEN, F.F. 1966 Microinstability and shear stabilization of a low-β, rotating, resistive plasma. *Phys. Fluids* **9** (5), 965–981.

ELLISON, C.L., RAITSES, Y. & FISCH, N.J. 2012 Cross-field electron transport induced by a rotating spoke in a cylindrical hall thruster. *Phys. Plasmas* **19** (1), 013503.

ESCARGUEL, A. 2010 Optical diagnostics of a low frequency instability rotating around a magnetized plasma column. *Eur. Phys. J.* D **56** (2), 209–214.

FRIDMAN, A.M. 1964 On the phenomena of the critical magnetic field and anomalous diffusion in weakly ionized plasma. *Sov. Phys. Dokl*. **9**, 75.

FURNO, I., AGNELLO, R., FANTZ, U., HOWLING, A., JACQUIER, R., MARINI, C., PLYUSHCHEV, G., GUITTIENNE, P. & SIMONIN, A. 2017 Helicon wave-generated plasmas for negative ion beams for fusion. In *EPJ Web of Conferences*, vol. 157. EDP Sciences.

GRAVIER, E., BROCHARD, F., BONHOMME, G., PIERRE, T. & BRIANÇON, J.L. 2004 Low-frequency instabilities in a laboratory magnetized plasma column. *Phys. Plasmas* **11** (2), 529–537.

GUEROULT, R., RAX, J.-M. & FISCH, N.J. 2017 Centrifugal instability in the regime of fast rotation. *Phys. Plasmas* **24** (8), 082102.

HOH, F.C. 1963 Simple picture of the finite larmor radius stabilization effect. *Phys. Fluids* **6** (9), 1359–1359.

ILIĆ, D.B., ROGNLIEN, T.D., SELF, S.A. & CRAWFORD, F.W. 1973 Low-frequency flute instabilities of a hollow cathode arc discharge: theory and experiment. *Phys. Fluids* **16** (7), 1042–1053.

JAEGER, S. 2010 Etude theorique et experimentale des instabilites basses frequences dans un plasma en champs magnetique et electrique croises. PhD thesis, Aix-Marseille University.

JASSBY, D.L. 1972 Transverse velocity shear instabilities within a magnetically confined plasma. *Phys. Fluids* **15** (9), 1590–1604.

LEHNERT, B. 1971 Rotating plasmas. *Nucl. Fusion* **11** (5), 485.

MATSUKUMA, M., PIERRE, T., ESCARGUEL, A., GUYOMARC'H, D., LECLERT, G., BROCHARD, F., GRAVIER, E. & KAWAI, Y. 2003 Spatiotemporal structure of low frequency waves in a magnetized plasma device. *Phys. Lett.* A **314** (1), 163–167.

PARKER, J.B., RAITSES, Y. & FISCH, N.J. 2010 Transition in electron transport in a cylindrical hall thruster. *Appl. Phys. Lett*. **97** (9).

PERKINS, F.W. & JASSBY, D.L. 1971 Velocity shear and low-frequency plasma instabilities. *Phys. Fluids* **14** (1), 102–115.

PIERRE, T. 2016 The slow collisional $e \times b$ ion drift characterized as the major instability mechanism of a poorly magnetized plasma column with an inward-directed radial electric field. *Phys. Plasmas* **23** (4), 042110.

PLIHON, N., BOUSSELIN, G., PALERMO, F., MORALES, J., BOS, W., GODEFERD, F., BOURGOIN, M., PINTON, J.-F., MOULIN, M. & AANESLAND, A. 2014 Flow dynamics and magnetic induction in the von-karman plasma experiment. *J. Plasma Phys*.

RAX, J.M., FRUCHTMAN, A., GUEROULT, R. & FISCH, N.J. 2015 Breakdown of the brillouin limit and classical fluxes in rotating collisional plasmas. *Phys. Plasmas* **22** (9), 092101.

ROGNLIEN, T.D. 1973 Low-frequency flute instabilities of a bounded plasma column. *J. Appl. Phys*. **44** (8), 3505–3512.

ROSENBLUTH, M.N., KRALL, N.A. & ROSTOKER, N. 1962 Finite larmor radius stabilization of "weakly" unstable confined plasmas. *Tech. Rep.* General Dynamics Corp.

SEKERAK, J.M., LONGMIER, W.B., GALLIMORE, A.D., BROWN, L.D., HOFER, R.R. & POLK, E.J. 2015 Azimuthal spoke propagation in hall effect thrusters. *IEEE Trans. Plasma Sci*. **43** (1), 72–85.

Smolyakov, A.I., Chapurin, O., Frias, W., Koshkarov, O., Romadanov, I., Tang, T., Umansky, M., Raitses, Y., Kaganovich, I.D. & Lakhin, V.P. 2016 Fluid theory and simulations of instabilities, turbulent transport and coherent structures in partially-magnetized plasmas of discharges. *Plasma Phys. Control. Fusion* **59** (1), 014041.

Stringer, T.E. & Schmidt, G. 1967 Flute instability in the presence of non-uniform electric fields. *Plasma Phys*. **9** (1).

Whittaker, E.T. & Watson, G.N. 1966 *A Course of Modern Analysis*. Cambridge University Press.

https://doi.org/10.1017/S002237782300051X Published online by Cambridge University Press